

# Geophysical Research Letters®

## RESEARCH LETTER

10.1029/2022GL098057

### Key Points:

- Shipboard, Deep-Argo, and mooring data capture a warming-to-cooling reversal of Lower North Atlantic Deep Water in the Irminger Sea in 2014
- The cooling trend is statistically significant and has likely accelerating in recent years, reaching  $-16 \pm 6 \text{ m}^\circ\text{C yr}^{-1}$  during 2016–2021
- Denmark Strait Overflow Water has warmed and cooled significantly faster than Iceland Scotland Overflow Water during 2002–2021

### Supporting Information:

Supporting Information may be found in the online version of this article.

### Correspondence to:








D. G. Desbruyères,  
[damien.desbruyeres@ifremer.fr](mailto:damien.desbruyeres@ifremer.fr)

### Citation:

Desbruyères, D. G., Bravo, E. P., Thierry, V., Mercier, H., Lherminier, P., Cabanes, C., et al. (2022). Warming-to-cooling reversal of overflow-derived water masses in the Irminger Sea during 2002–2021. *Geophysical Research Letters*, 49, e2022GL098057. <https://doi.org/10.1029/2022GL098057>

Received 27 JAN 2022  
Accepted 5 MAY 2022

## Warming-to-Cooling Reversal of Overflow-Derived Water Masses in the Irminger Sea During 2002–2021

Damien G. Desbruyères<sup>1</sup> , Eva Prieto Bravo<sup>1</sup>, Virginie Thierry<sup>1</sup> ,  
Herlé Mercier<sup>1</sup> , Pascale Lherminier<sup>1</sup> , Cécile Cabanes<sup>1</sup>, Tiago C. Biló<sup>2</sup> , Nora Fried<sup>3</sup> , and  
M. Femke De Jong<sup>3</sup> 

<sup>1</sup>University of Brest, CNRS, Ifremer, IRD, Laboratoire d'Océanographie Physique et Spatiale (UMR, LOPS), Plouzané 6523, France, <sup>2</sup>Scripps Institution of Oceanography, University of California San Diego, La Jolla, CA, USA, <sup>3</sup>Department of Ocean Systems, NIOZ, Royal Netherlands Institute for Sea Research, Texel, The Netherlands

**Abstract** Shipboard hydrography along the A25-Ovide section (2002–2018) is combined with a high-resolution mooring array (2014–2020) and a regional fleet of Deep-Argo floats (2016–2021) to describe temperature changes of overflow-derived water masses in the Irminger Sea. Removing dynamical influences enables to identify a new statistically significant trend reversal in Iceland Scotland Overflow Water (ISOW) and Denmark Strait Overflow Water (DSOW) core temperatures in the mid-2010s. A basin-wide cooling trend of  $-16 \pm 6 \text{ m}^\circ\text{C yr}^{-1}$  during 2016–2021—but reaching as strong as  $-44 \pm 13 \text{ m}^\circ\text{C yr}^{-1}$  for DSOW in recent years—is found to interrupt a warming phase that was prevailing since the late 1990s. The absence of an apparent reversal in the Nordic Seas and the faster changes detected in DSOW compared to ISOW point out the entrainment of subpolar signals within the overflows near the Greenland-Iceland-Scotland sills as a most likely driver.

**Plain Language Summary** The North Atlantic Deep Water is one of the most voluminous water masses of the global ocean. Its deepest constituent—the Lower North Atlantic Deep Water (LNADW)—forms in the Nordic Seas before cascading into the North Atlantic at the Greenland-Iceland-Scotland sills and progressing south toward the Southern Ocean. The temperature and salinity of LNADW are known to obey decadal trends in response to forcing in its source regions as well as subsequent mixing with surrounding and overlying water masses during its Atlantic journey. Here, repeated measurements from oceanographic vessels, continuous monitoring with moored instrumentations, and autonomous Deep-Argo floats in the Irminger Sea (east of Greenland) during 2002–2021 are used to reveal a new warming-to-cooling reversal of LNADW in 2014. This signal, which presumably originates in the entrainment of upper and intermediate ocean variability near the Greenland-Iceland-Scotland sills, will progressively travel southward within the lower branch of the Atlantic Meridional Overturning Circulation.

## 1. Introduction

The warming of the global ocean remains an unabated consequence of human-driven climate change (IPCC et al., 2021). The progressive rise in atmospheric greenhouse gas concentrations causes an extra downward heat flux of about  $0.6\text{--}0.8 \text{ W m}^{-2}$  through the sea surface (Desbruyères et al., 2017; Johnson et al., 2016), with a likely acceleration in recent years (Von Schuckmann et al., 2020) and several ramifications on sea level rise (Tebaldi et al., 2021), ocean stratification and mixing processes (Sallée et al., 2021), or ocean deoxygenation and carbon sequestration (Keeling et al., 2009). This global warming rate is often inferred from in situ observations of ocean heat content, which became well constrained in the mid-2000s owing to the completed implementation of the global network of 0–2,000 m Argo profiling platforms (Riser et al., 2016). A significant source of uncertainty on global and regional OHC increase remains however linked to the comparatively poor systematic and homogeneous sampling of the deep ocean below 2,000 (Garry et al., 2019; Purkey & Johnson, 2010). This issue contributed to motivate the deep extension of the Argo array since the mid 2010s, the Deep-Argo program (Johnson et al., 2015; Roemmich et al., 2019).

Key regions for deep ocean heat storage variability were targeted to conduct Deep-Argo pilot experiments. One of them is the Subpolar North Atlantic Ocean (SPNA) where a cold and dense water mass—the North Atlantic Deep Water (NADW)—constantly propagates interannual to multi-decadal thermohaline and biogeochemical

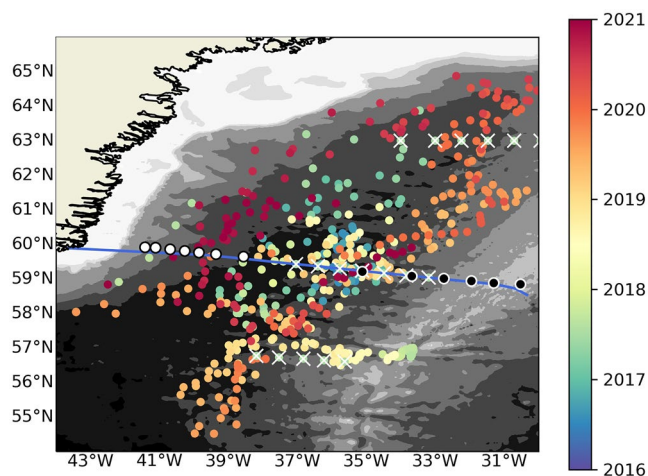


**Figure 1.** Study domain along with the A25-Ovide section (blue line), RREX 2017 (white crosses), WI and EI OSNAP mooring locations (white and black circles, respectively), and Deep-Argo floats profiles with dots colored by their decimal year. Background shading is 500 m spaced isobaths.

signals over large spatial scales (Talley et al., 2011). The climatic significance of NADW is also witnessed by the on going deployment of a Canada—Greenland—Scotland mooring array (the Overturning in the Subpolar North Atlantic Program; OSNAP), which enables since 2014 a continuous monitoring of its thermohaline properties and volume transport (Lozier et al., 2019). However, while much is known about the intrinsic variability of upper NADW formed in the SPNA through deep convective mixing because of efficient monitoring with core Argo floats above 2,000 m (Yashayaev & Loder, 2016), local thermohaline changes within the lower NADW (LNADW) that originates in the Nordic Seas has received less attention in the recent literature.

The LNADW is convectively formed in the Greenland and Norwegian Seas and enters the subpolar North Atlantic via narrow cascading flows constrained by the shallow ridge (<1,000 m) that extends from Scotland to Greenland (Hansen & Østerhus, 2000). As it overflows, LNADW entrains surrounding and mixes with, less dense, Atlantic waters to form overflow-derived water masses, namely the Iceland-Scotland Overflow Water (ISOW) and the Denmark Strait Overflow Water (DSOW). Dickson et al. (2002) reported on a long-term (1965–2002) gradual freshening of both overflow-derived water masses in the Irminger and Labrador Seas. This was partly attributed to an upstream freshening of the source waters in the Nordic Seas, and partly to mixing with upper and intermediate water masses southeast of Iceland and

in the Irminger Seas that were themselves freshening at equal or greater rates. A reversal of this trend in the late 1990's was subsequently observed, with ISOW and DSOW entering a warming and salinification phase until the year 2006 at least (Holliday et al., 2008; Sarafanov et al., 2010, 2007; van Aken & de Jong, 2012). Here, we pursue those efforts and analyze the recent variability in ISOW and DSOW properties in the Irminger Sea using nine biennial occupations (2002–2018) of the Portugal-Greenland A25-Ovide section (Daniault et al., 2016; Mercier et al., 2015), the 2017 occupation of the Reykjanes Ridge Experiment (RREX) sections (Petit et al., 2018), 6 yr of OSNAP mooring data (2014–2020), and about 6 yr (2016–2021) of continuous Deep-Argo observations. We report LNADW temperature changes in the Irminger Sea and discuss their likely drivers, distinguishing local dynamical signatures from intrinsic ISOW and DSOW anomalies. We also further demonstrate the high scientific value of sustained a Deep-Argo array (Foppert et al., 2021; Johnson, 2019; Johnson et al., 2020; Kobayashi, 2018; Racapé et al., 2019; Zilberman et al., 2020), and to particularly highlight its usefulness alongside repeat shipboard hydrography and moored instrumentations for a comprehensive monitoring of deep temperature changes. The data sets and the methodology are described in Section 2. Results are provided in Section 3 and summarized and discussed in Section 4.

## 2. Materials and Methods

### 2.1. Repeat Hydrography, Deep-Argo, and OSNAP Data Sets

The geographical distribution of all profiles (i.e., shipboard and floats) and the location of moorings is shown in Figure 1. Nine years of hydrographic data were provided by biennial (summer) repetitions of the Greenland-Portugal A25-Ovide line from 2002 to 2018 (Daniault et al., 2016). Gridded fields of temperature and salinity (1 db  $\times$  7 km) were interpolated linearly on an annual grid to derive 2005–2017 climatological fields and allow consistent comparisons with the concomitant World Ocean Atlas 2018 climatology (see below). Additional shipboard hydrography profiles gathered along the eastern flank of the Reykjanes Ridge in 2017 were also used (Petit et al., 2018), as well as 484 full-depth temperature and salinity profiles provided by eight Deep-Argo floats deployed in the Irminger Basin through 2016–2021. Those were quality-controlled and salinity was adjusted to reference profiles following the procedure specified for Deep-Argo floats (Wong et al., 2021).

The OSNAP data sets consist of two mooring arrays covering the western flank of the Reykjanes Ridge (OSNAP-EI hereafter) and the Irminger Sea's western boundary (OSNAP-WI hereafter). All moorings measured hydrographic properties every 15 min to 1 hr July–August 2014 and July 2020. Below 1,000 m, these instruments are vertically separated by a few hundreds of meters. In the present study, moored calibrated temperature and salinity data were low-pass filtered using a 41 hr sixth-order Butterworth filter and subsampled to daily

resolution. Hydrographic fields were then vertically (horizontally) interpolated onto regular grids using a piecewise Hermite cubic polynomial (linear) interpolation schemes. Additional information on OSNAP data calibration procedures, processing, and interpolation are already published (de Jong et al., 2020; Fried & de Jong, 2022; Johns et al., 2021; Le Bras et al., 2018).

## 2.2. WOA18 and OV18 Climatologies

The 2005–2017 climatology of temperature ( $\theta$ ) in the Irminger Basin (30°–44°W, 54°–66°N) was extracted from the 1/4° global World Ocean Atlas 2018 (WOA18). Using this most recent decade as a climatological baseline should minimize the risk of aliasing spatial and temporal variability due to sparse and non-regular data distribution. To further evaluate this risk, we follow Kobayashi (2018) and construct an independent regional climatology from the well-constrained 2005–2017 mean A25-Ovide  $\theta$  field. This construction assumes along-isopycnal potential vorticity ( $f/H$ ) conservation as water masses flow cyclonically in the Irminger Sea (where  $f$  is the Coriolis parameter and  $H$  the ocean depth, here obtained from a smoothed version of the 2' ETOPO topography). North of A25-Ovide, the climatological temperature along a given  $f/H$  contours was estimated as:

$$\langle \theta_{f/H} \rangle = (1 - l) * \langle \theta_W^{A25} \rangle + l * \langle \theta_E^{A25} \rangle \quad (1)$$

where  $\langle \theta_W^{A25} \rangle$  and  $\langle \theta_E^{A25} \rangle$  are the climatological temperature at the western and eastern intersections of the  $f/H$  contour with the section, and  $l$  is a weight calculated from the along-contour distance between the western intersection and the point on the  $f/H$  contour where the estimation is to be made (divided by the total length of the contour). South of A25-Ovide, the climatological temperature along a given  $f/H$  contours was set from the closest intersection of this  $f/H$  contour with the section. We will refer to this A25-Ovide climatological product as OV18 hereafter.

## 2.3. Heave and Spice

An isopycnal decomposition of  $\theta$  anomalies into  $\theta_{\text{HEAVE}}$  (anomalies at a fixed pressure associated with isopycnal displacements) and  $\theta_{\text{SPICE}}$  (anomalies on potential density surfaces) is carried out (Bindoff & McDougall, 1994). Temperature and pressure profiles were interpolated onto a 0.001-resolution  $\sigma_2$  vertical grid. Temperature anomalies on fixed  $\sigma_2$  surfaces yield the  $\theta_{\text{SPICE}}$  component in  $\sigma_2$  space, while pressure anomalies at fixed  $\sigma_2$  surfaces multiplied by the local vertical background temperature gradient yield the  $\theta_{\text{HEAVE}}$  component in  $\sigma_2$  space. Both components are eventually re-gridded on a uniform grid at 10 dbar intervals using the pressure of  $\sigma_2$  surfaces, and the departure of their sum from the true anomalies or trends provide the error of the decomposition. This method has been regularly applied in water mass analyses in the North Atlantic as an indicative means to infer the sources or mechanisms of the observed changes (e.g., Häkkinen et al., 2015). Here, we will interpret  $\theta_{\text{SPICE}}$  as the advection of a remote thermohaline signals within ISOW and DSOW (e.g., due to anomalous air-sea heat exchanges in the Nordic Seas, or to the entrainment of anomalies from overlying layers near the sills). On the other hand,  $\theta_{\text{HEAVE}}$  will be interpreted as remote changes in ISOW and/or DSOW formation rates or local dynamical changes (e.g., wind-driven lateral shift of geostrophic currents). We will primarily focus on  $\theta_{\text{SPICE}}$ , and consider  $\theta_{\text{HEAVE}}$  as the dynamical signal to be removed to reveal intrinsic water mass property changes.

## 2.4. Linear Trends and Uncertainties From Float Data

We compute linear  $\theta$  trends and associated uncertainties from Deep-Argo observations following Johnson et al. (2019). Trends are computed at each pressure levels from all profiles regardless of their location, with standard errors and 95% confidence intervals derived from the residuals to the linear fit using standard methodology for unweighted least squares regressions. To do so, we obtain the number of degrees of freedom at each pressure level by assuming that all floats are statistically independent of each other (i.e., that their horizontal separation length scales are greater than that of the dominant transient features in the region, typically eddies). However, time series from individual floats are serially correlated, and a typical decorrelation length scale of 60 days computed globally from Argo data at 1,800 db is used (Johnson et al., 2015), and assumed to prevail at greater depth due to the vertically uniform banded structure of  $\theta$  trends observed in the region (Desbruyères et al., 2014).

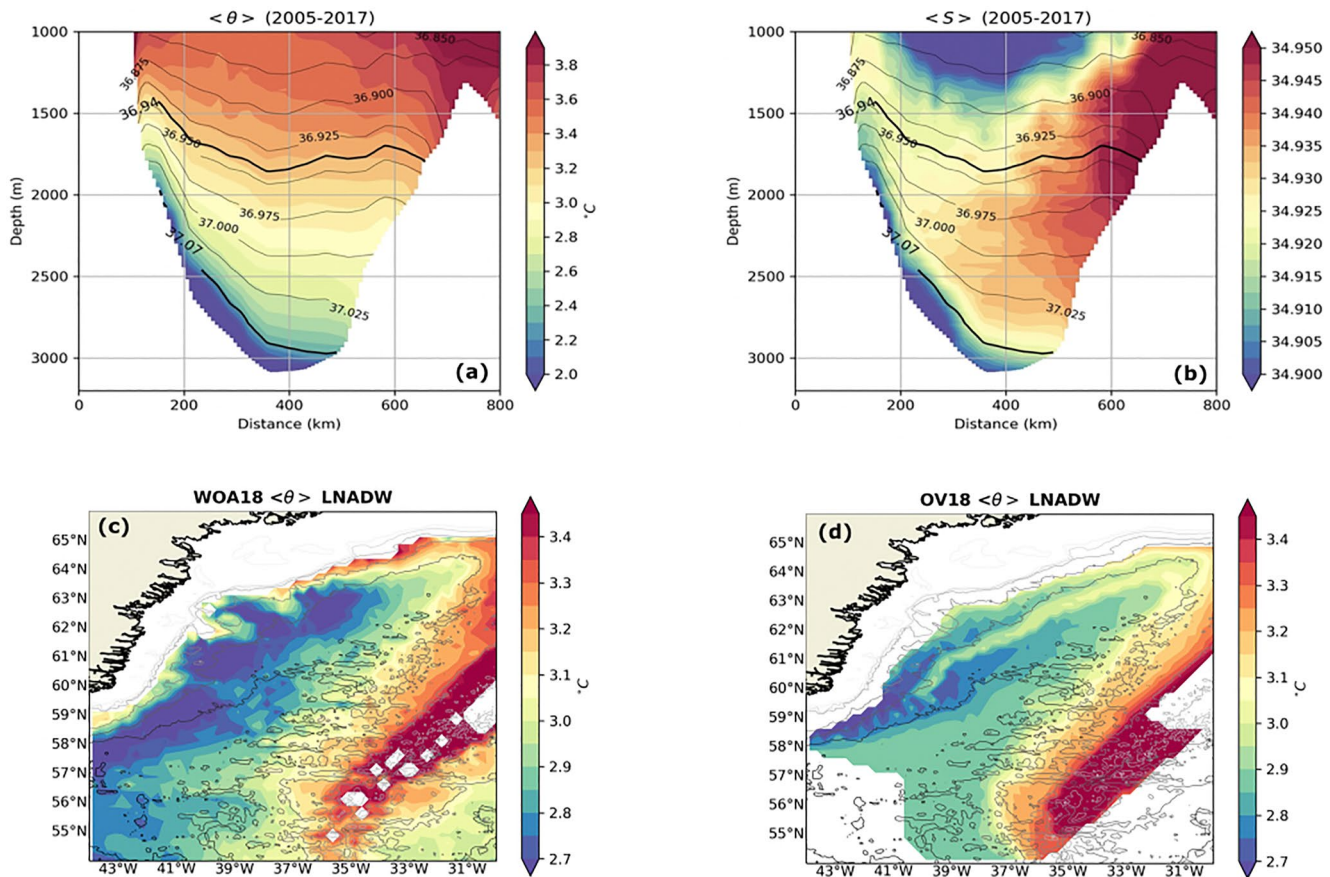


**Figure 2.** Climatological mean (2005–2017) of (a) conservative temperature and (b) salinity at the A25-Ovide section. Thin black lines show isopycnal  $\sigma_2$  surfaces and thick black lines show  $\sigma_2 = 36.94$  and  $\sigma_2 = 37.07$  that are respectively used as an upper bound for LNADW and as a lower (upper) bound for ISOW (DSOW). (c) The 2005–2017 WOA18 field of conservative temperature averaged within the LNADW layer (i.e., below  $\sigma_2 = 36.94$ ). (d) same as (c) but from OV18.

### 3. Results

#### 3.1. The Climatological Picture

The deep stratification is dominated by  $\theta$ , with an east-west asymmetry associated with the northward advection of relatively warm waters at mid-depth along the western flank of Reykjanes Ridge and the southward advection of relatively cold waters along the deepest portion of Greenland continental slope (Figure 2a). The presence of baroclinic boundary currents is revealed by the inshore plunging of isopycnal surfaces above 2,000 m on both side of the basin. The salinity section depicts the predominant salty signature of ISOW spreading offshore from Reykjanes Ridge, and the fresh signatures of LSW above 1,500 m in the interior and of DSOW above the western continental slope (Figure 2b). In the following, only the water masses denser than  $\sigma_2 = 36.94$  ( $\sim\sigma_0 = 27.80$ ) will be considered in order to willingly exclude LSW signals and focus the analysis on LNADW, which will be decomposed into ISOW and DSOW using  $\sigma_2 = 37.07$  ( $\sim\sigma_0 = 27.88$ ; Danialt et al., 2016).

The WOA18 and OV18 climatological fields of  $\theta$  vertically averaged within LNADW are shown in Figures 2c and 2d, respectively. They both capture a broad warm-to-cold transition of the boundary current, which is broader and patchier in WOA18 owing to the relatively coarse horizontal length scales used in the interpolation scheme as well as the underlying uneven data distribution. OV18 shows a thinner and gradually cooling boundary current as expected from the simple linear model (Equation 1). A second, maybe more striking, difference is a colder western basin interior in WOA18 than in OV18, which reflects the lacking signature of DSOW inflow from Denmark Strait in the OV18 reconstruction (not shown). WOA18 and OV18 have been used side-by-side in Section 3.3 and Section 3.4 to estimate temperature anomalies from Deep-Argo profiles. Their discrepancies were most exclusively reflected in  $\theta_{\text{HEAVE}}$  due to the dependence of this component to the background stratification. Because



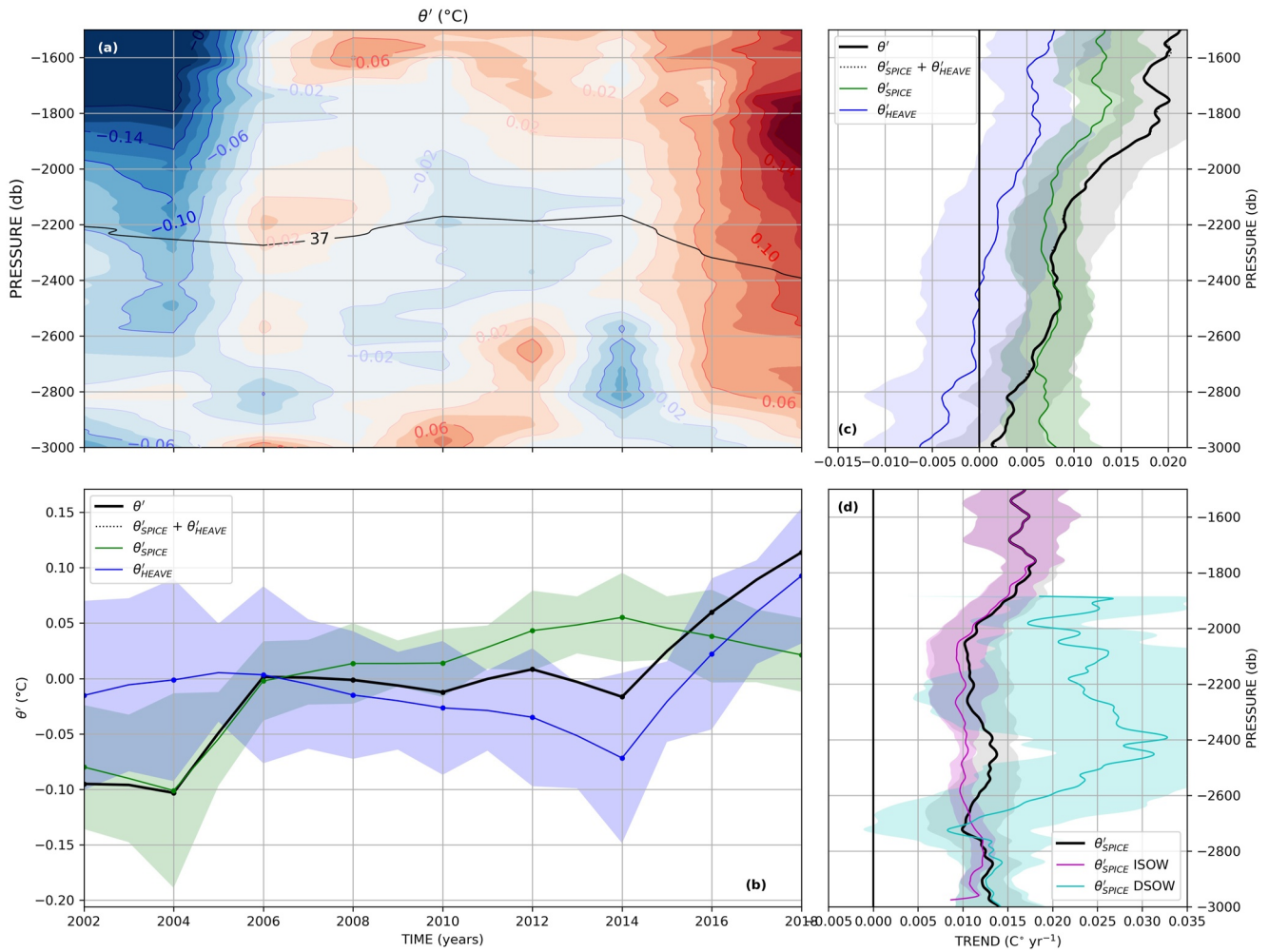


**Figure 3.** A25-Ovide analysis (2002–2018). (a). Horizontally averaged temperature anomalies within the LNADW layer (relative to the 2005–2017 period) at the A25-Ovide section. The black line shows  $\sigma_2 = 37 \text{ kg m}^{-3}$ . (b) Temperature anomalies averaged within the LNADW layer (black) and decomposed into  $\theta_{\text{SPICE}}$  and  $\theta_{\text{HEAVE}}$  (green and blue, respectively). Their sum is shown with the dotted line and their respective spatial standard deviations are shaded. (c) The 2002–2018 linear temperature trends as a function of pressure averaged within the LNADW layer for each component ( $^{\circ}\text{C yr}^{-1}$ ). (d) The 2002–2014 linear  $\theta_{\text{SPICE}}$  trends as a function of pressure averaged within the whole LNADW layer (black), within the ISOW layer (magenta), and within the DSOW layer (cyan). In both (c and d) shadings indicate 5%–95% confidence limits.

results were on the other hand markedly similar for  $\theta_{\text{SPICE}}$ —our focus herein—OV18-based diagnostics will be provided as Supporting Information.

### 3.2. Long-Term Changes Measured at the A25-Ovide Section

The 2002–2018 A25-Ovide data set provides a local yet a long-term time series of LNADW  $\theta$  anomalies in the Irminger Sea. It shows a period of anomalously cold conditions (2002–2006) and a period of anomalously warm condition (2014–2018) separated by a period of weak changes (2006–2014; Figures 3a and 3b). The horizontally averaged trend during 2002–2018 shows statistically significant warming over most of the LNADW vertical extent with a gradual decrease in magnitude from a maximum of  $20 \text{ m}^{\circ}\text{C yr}^{-1}$  at 1,500 m to near zero at 3,000 m, and a depth-averaged value of  $10 \pm 4 \text{ m}^{\circ}\text{C yr}^{-1}$  (black line in Figure 3c).

Decomposing  $\theta$  anomalies into  $\theta_{\text{SPICE}}$  and  $\theta_{\text{HEAVE}}$  provides the fraction of the observed changes driven by actual water mass property changes.  $\theta_{\text{SPICE}}$  anomalies increased sharply between 2004 and 2006 before gradually increasing at a slower rate until 2014 when cooling conditions appeared (green line in Figure 3b). The horizontally averaged  $\theta_{\text{SPICE}}$  trend is positive and statistically significant at all depths, with a depth-averaged value of

$8 \pm 3 \text{ m}^\circ\text{C yr}^{-1}$  (green line in Figure 3c). On the other hand,  $\theta_{\text{HEAVE}}$  is characterized by a gradual cooling between 2006 and 2014 and a sharp warming afterward (blue line in Figure 3b). This can be also visualized with the changing depth of  $\sigma_2 = 37$ —an isopycnal surface falling within the core of LNADW (black line in Figure 3a). The depth-averaged  $\theta_{\text{HEAVE}}$  trend is relatively weak ( $2 \pm 5 \text{ m}^\circ\text{C yr}^{-1}$ ) due to a compensation between warming within the 1,500–2,400 m layer and cooling below, which is seemingly in line with an adiabatic redistribution of water masses (blue line in Figure 3c). Statistical significance is not reached except near 1,800 m. Overall, LNADW in the Irminger Sea appear to have significantly warmed during 2002–2018 at all depth levels, while local and/or remote dynamical changes enhanced and reduced warming rates at constant pressure above and below 2,400 m, respectively. Trends reversed in 2014 however, with a sharp downward displacement of isopycnal surfaces (supposedly driven by lateral shift of geostrophic fronts at the boundaries—not shown) masking a return to a density-compensated cooling phase for LNADW. This is further described below with the Deep-Argo and OSNAP data sets.

### 3.3. Recent Changes Measured by Deep-Argo Floats and the OSNAP Mooring Array

Recurrent  $\theta$  and  $S$  measurements in the Irminger Sea by Deep-Argo floats (plus the 2017 RREX hydrography survey) provide key basin-scale information in recent years. During 2016–2021, most of the LNADW layer in the Irminger Sea was significantly warmer than during 2005–2017, although cold LNADW anomalies are sporadically found along the boundaries of the basin (Figure 4a). The 2016–2021 linear trend and its 95% confidence interval at each pressure level within the LNADW layer is shown in Figure 4c (black line). Its depth-averaged magnitude of  $-17 \pm 19 \text{ m}^\circ\text{C yr}^{-1}$  hides a complicated vertical structure with statistical significance restricted to those small portions of the water column where the trend magnitude is peaking (e.g., 1,600, 2,100, and 2,800 m). Again, the isopycnal decomposition reveals a key role for  $\theta_{\text{HEAVE}}$  in dictating this vertical structure, with peaking intensity potentially reflecting local volume changes of ISOW and DSOW (blue line in Figure 4c). Most importantly, the trend in  $\theta_{\text{SPICE}}$  is uniformly negative and statistically significant, with a depth-averaged trend of  $-16 \pm 6 \text{ m}^\circ\text{C yr}^{-1}$  and bottom-intensified cooling rates up to  $60 \text{ m}^\circ\text{C yr}^{-1}$  (green line in Figure 4c). This shows the persistence of the warming-to-cooling reversal in LNADW core temperature detected along A25-Ovide since 2014 (Figure 3b).

The horizontal pattern of  $\theta_{\text{SPICE}}$  anomalies derived from Deep-Argo profiles is moreover illuminating (Figure 4b). It shows a clear contrast between positive anomalies covering a broad area of the basin interior, weakly positive and negative anomalies along the flank of Reykjanes Ridge, and large negative anomalies off Greenland. This indicates that the 2014–2021 cooling trend of LNADW first appeared along the boundary of the basin before progressively spreading into the interior, in line with the remote advection of colder LNADW classes by the mean boundary-focused circulation. It also suggests a most significant decrease of DSOW temperature in recent years, as discussed in Section 3.4.

Finally, OSNAP-WI and OSNAP-EI provide a more local but higher-resolution boundary-focused measurements during 2014–2020 and therefore a third independent estimate of LNADW variability. Applying the isopycnal decomposition to gridded  $\theta$  and  $S$  fields confirms the statistically significant cooling of LNADW at both the western and eastern side of the basin (Figures 4e and 4g, respectively), as well as the tendency for isopycnal heave to oppose and mask this intrinsic trend in water mass property. The magnitude of mooring-based  $\theta_{\text{HEAVE}}$  trends can be expectedly relatively large (e.g.,  $25 \pm 9 \text{ m}^\circ\text{C yr}^{-1}$  for OSNAP-WI), since moorings predominantly sample the highly dynamical boundary region where lateral geostrophic shifts and temperature gradients (and hence isopycnal heave) are most significant. Most importantly, the magnitudes of  $\theta_{\text{SPICE}}$  trends are quantitatively in line with those captured by Deep-Argo during 2016–2021, respectively reaching  $-12 \pm 3$  and  $-16 \pm 5 \text{ m}^\circ\text{C yr}^{-1}$  across the OSNAP-WI and OSNAP-EI.

### 3.4. ISOW and DSOW Contributions

We eventually quantify the respective signature of ISOW and DSOW on the observed LNADW  $\theta_{\text{SPICE}}$  trends and, in particular, on the Ovide-based warming phase (Figure 3d), and on the Deep-Argo-based, OSNAP-WI-based, and OSNAP-EI-based cooling phases (Figures 4d, 4f, and 4h, respectively). During 2002–2014, ISOW warmed at a depth-averaged rate of  $12 \pm 2 \text{ m}^\circ\text{C yr}^{-1}$ , before cooling at a rate of  $-11 \pm 6 \text{ m}^\circ\text{C yr}^{-1}$  during 2016–2021 (Deep-Argo). Consistently, ISOW cooling rates measured at OSNAP-WI and OSNAP-EI during 2014–2020 were

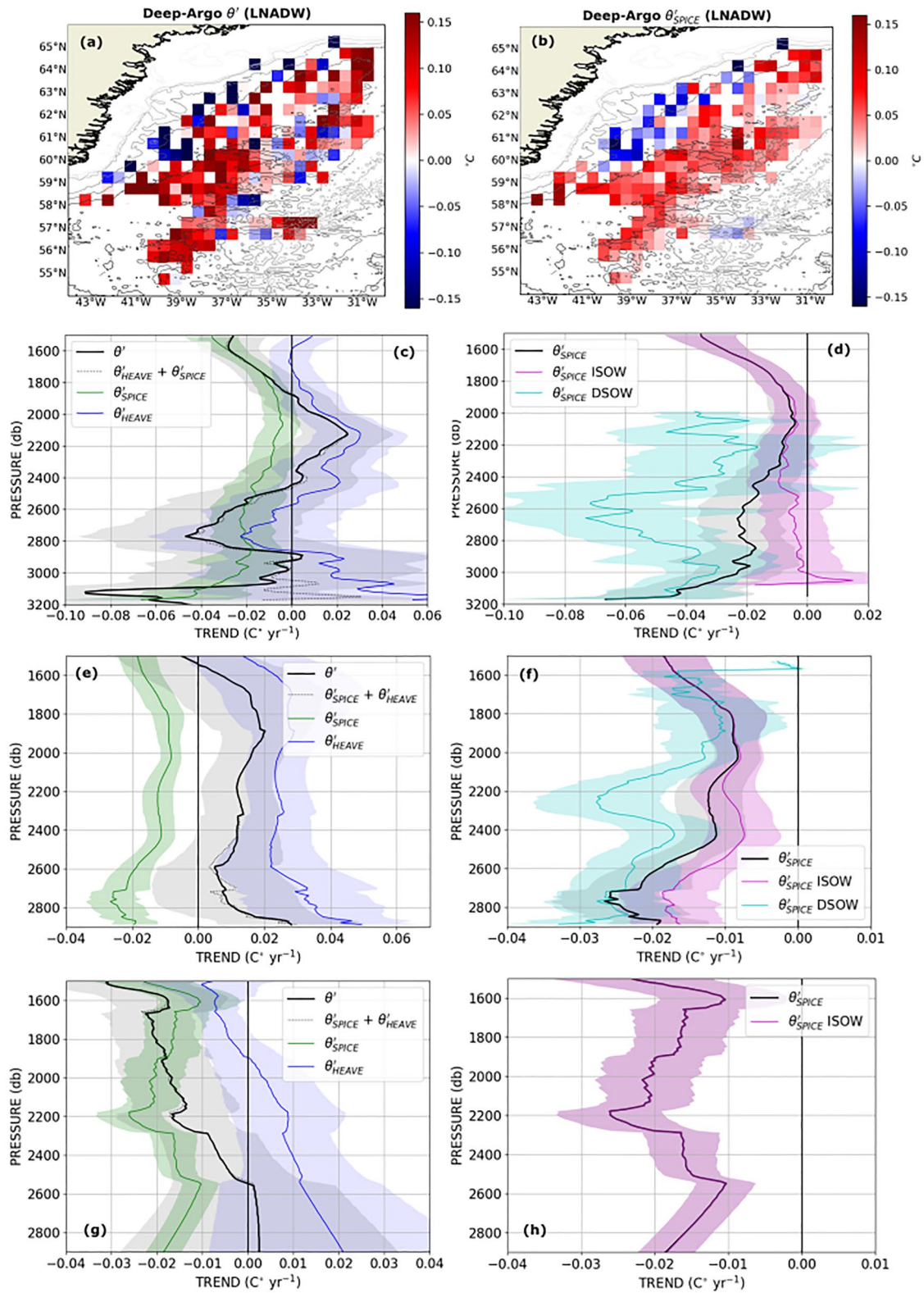


Figure 4.

$-10 \pm 3$  and  $-16 \pm 5$   $\text{m}^\circ\text{C yr}^{-1}$ , respectively. The magnitudes of DSOW  $\theta_{\text{SPICE}}$  trends were significantly larger, with a warming rate of  $18 \pm 8$   $\text{m}^\circ\text{C yr}^{-1}$  during 2002–2014 and cooling rates of  $-22 \pm 6$   $\text{m}^\circ\text{C yr}^{-1}$  during 2014–2020 at OSNAP-WI and of up to  $-44 \pm 13$   $\text{m}^\circ\text{C yr}^{-1}$  during 2016–2021 basin wide. This apparent acceleration of the cooling trend is confirmed by computing the linear trend at OSNAP-WI during 2017–2020 (i.e., close to the Deep-Argo time-span). The latter yields a rate of  $-38 \pm 9$   $\text{m}^\circ\text{C yr}^{-1}$ , in good agreement with the independent Deep-Argo-based estimate.

#### 4. Conclusion and Discussion

The deep layer of the Irminger Sea ( $\sim 1,500$ – $3,000$  m) underwent positive and negative temperature trends over the last two decades (2002–2021) that were one order of magnitude larger than global and basin-scale estimates within the same layer (Desbruyères et al., 2016). After removing heave-induced signals, which most likely reflect wind-driven and/or buoyancy-driven geostrophic adjustments of boundary currents and possibly water mass volume changes, we report from three independent data sets (shipboard hydrography, Deep-Argo floats, and OSNAP moorings) a statistically-significant warming-to-cooling reversal in the core temperature of overflow-derived water masses in the mid-2010's. The LNADW warmed during 2002–2014 at an average rate of  $13 \pm 3$   $\text{m}^\circ\text{C yr}^{-1}$  and is cooling since then, with a suggested accelerating rate of change reaching  $-16 \pm 6$   $\text{m}^\circ\text{C yr}^{-1}$  during 2016–2021. While those trends were consistently detected within the two components of LNADW, their magnitudes were significantly larger for DSOW than for ISOW, with their ongoing cooling notably reaching average rates of  $-44 \pm 13$  and  $-11 \pm 6$   $\text{m}^\circ\text{C yr}^{-1}$ , respectively.

Investigating the causes of the observed changes is beyond the scope of this descriptive study but the patterns we report and the relevant literature can already enable a tentative explanation. While the gradual warming of ISOW and DSOW in the Irminger Sea during 2002–2014 is not inconsistent with the reported steady warming of the Nordic Seas, there has not been clear signs of sustained cooling in recent years in this source region (Broomé et al., 2020). This suggests that the 2014 warming-to-cooling reversal of ISOW and DSOW was most likely driven by the entrainment of SPNA signals within the overflow plumes at the Greenland-Iceland-Scotland sills and isopycnal mixing with intermediate waters further downstream. This mechanism was already advocated by Dickson et al. (2002) for the preceding 1960s–1990s cooling and freshening phase, by Sarafanov et al. (2010) for the subsequent warming and salinification phase (1990s–2000s), and most recently to explain the substantial freshening of ISOW in the Iceland Basin (Devana et al., 2021). Such an entrainment-mixing pathway for decadal thermohaline signals is in fact consistent with the recent history of both upper water mass property changes and LSW property changes in the SPNA, which entered a cooling (and freshening) phase circa 2006 and 2012, respectively (Desbruyères et al., 2021; Piron et al., 2017; Robson et al., 2016; Yashayaev & Loder, 2017). This mechanism also concurs with the striking differences in trend magnitudes between ISOW and DSOW. Those differences can be expected from the reported shift in the deep convection pattern toward the Irminger Sea in recent years (Rühs et al., 2021), from the relatively higher dilution of LSW signals between the Labrador Sea and the Iceland-Scotland sills (as compared to the Greenland—Iceland sill), and from isopycnal and diapycnal mixing diluting ISOW signals before it actually enters the Irminger domain (Petit et al., 2018; Racapé et al., 2019).

On top of accounting for a non-negligible fraction of the full water column heat content in the Irminger Sea, the temperature trends affecting ISOW and DSOW can have far-reaching impacts on the dynamics of the North Atlantic, including that of its Meridional Overturning Circulation (MOC) whose variability is intimately linked to thermohaline anomalies propagating along the western boundary of the domain (Buckley & Marshall, 2016; Waldman et al., 2020). Specifically, the expected downstream advection within the deep western boundary current of the warming-to-cooling reversal observed herein would in theory imply an intensification of the basin-wide geostrophic shear and hence on the overturning strength. The actual fate of such anomalies as they travel and mix around during their southward journey, including their degree of density-compensation and therefore

**Figure 4.** Deep-Argo (2016–2021) and OSNAP analysis (2014–2020). (a) The 2016–2021 Deep Argo-based temperature anomalies relative to the 2005–2017 WOA18 climatology and averaged within the LNADW layer (i.e., below  $\sigma_2 = 36.94$ ). Profiles were gridded at  $1/4^\circ$  resolution for clarity. (b) same as (a) but for  $\theta_{\text{SPICE}}$ . (c) The linear temperature trends during 2016–2021 as a function of pressure averaged within the whole LNADW layer (black) decomposed into  $\theta_{\text{SPICE}}$  and  $\theta_{\text{HEAVE}}$  (green and blue, respectively, with their sum shown with the dotted line). (d) The 2016–2021 linear  $\theta_{\text{SPICE}}$  trend as a function of pressure averaged within the whole LNADW layer (black), within the ISOW layer (magenta), and within the DSOW layer (cyan). (e, f) and (g, h) same as (c, d) but from the OSNAP-WI and OSNAP-EI data sets, respectively. Shadings indicate 5%–95% confidence limits.



the influence they can have on a meridionally coherent mode of MOC variability, remains a motive of current active research.

## Data Availability Statement

The 1/4° global World Ocean Atlas 2018 (WOA18) was obtained online at <https://www.ncei.noaa.gov/data/oceans/woa/WOA18/DATA/>. The A25-Ovide sections (2002–2018) are available <https://doi.org/10.17882/46448>. All bottle files (2002–2018) are available via the Global Ocean Data Analysis Project (GLODAP) hosted by the Ocean Carbon and Acidification Data System (OCADS) at [https://www.ncei.noaa.gov/access/ocean-carbon-acidification-data-system/oceans/RepeatSections/clivar\\_ovide.html](https://www.ncei.noaa.gov/access/ocean-carbon-acidification-data-system/oceans/RepeatSections/clivar_ovide.html). The Argo data were collected and made freely available by the International Argo Program and the national programs that contribute to it (<https://argo.ucsd.edu>, <https://www.ocean-ops.org/board>). The Argo Program is part of the Global Ocean Observing System. The Deep-Argo data used herein are included in the 10 January 2022 snapshot of the Global Data Assembly Center (Argo GDAC) available via <http://doi.org/10.17882/42182#90708>. Data for the OSNAP-EI array are available via <https://doi.org/10.25850/nioz/7b.b.rb> (2014–2015), <https://doi.org/10.25850/nioz/7b.b.sb> (2015–2016), <https://doi.org/10.25850/nioz/7b.b.nb> (2016–2018), <https://doi.org/10.25850/nioz/7b.b.pb> (2018–2020).

## Acknowledgments

This work has received funding from the European Union's Horizon 2020 Research and Innovation Program under grant agreement n°824131 (Euro-Argo RISE project) and was carried out within the framework of the NAOS and ARGO-2030 projects. The two projects received the support of the French government within the framework of the “Investissements d'avenir” program managed by the Agence Nationale de la Recherche (ANR) under the references ANR-10-EQPX-40 and ANR-21-ESRE-0019. The authors thank all colleagues and ship crews involved in the Ovide and RREX cruises during which the hydrography data and Deep-Argo floats used in this study were obtained and deployed, respectively. The RREX project was funded by IFREMER, the Institut National des Sciences de l'Univers—Les enveloppes fluides et l'Environnement, Région Bretagne, Conseil Général du Finistère, and Brest Métropole. The OVIDE project was supported by CNRS, Ifremer, the national program LEFE (Les Enveloppes Fluides et l'Environnement), PICS (Projet International de Coopération Scientifique) No. 6058 and the Spanish Ministry of Sciences and Innovation co-funded by the Fondo Europeo de Desarrollo Regional 2007–2012 (FEDER) through the CATARINA project (CTM2010-17141). This work has been supported by BOCATS2 (PID2019-104279GB-C21) project funded by MCIN/AEI/10.13039/501100011033. The authors acknowledge the use of data from the international OSNAP program. OSNAP IC mooring is funded by Horizon 2020 Research and Innovation Program under Grant 727852 (Blue-Action). OSNAP DWBC moorings are funded in part by the U.S. National Science Foundation under WHOI grants OCE-1756363 and OCE-1948505. TCB was funded by National Science Foundation under grants OCE-1258823 and OCE-1756272. The authors thank Penny Holliday, Fiamma Straneo, and Amy Bower for their guidance in incorporating OSNAP data in this analysis.

## References

- Bindoff, N. L., & McDougall, T. J. (1994). Diagnosing climate change and ocean ventilation using hydrographic data. *Journal of Physical Oceanography*, 24(6), 1137–1152. [https://doi.org/10.1175/1520-0485\(1994\)024<1137:DCCA0V>2.0.CO;2](https://doi.org/10.1175/1520-0485(1994)024<1137:DCCA0V>2.0.CO;2)
- Broomé, S., Chafik, L., & Nilsson, J. (2020). Mechanisms of decadal changes in sea surface height and heat content in the eastern Nordic Seas. *Ocean Science*, 16(3), 715–728. <https://doi.org/10.5194/os-16-715-2020>
- Buckley, M. W., & Marshall, J. (2016). Observations, inferences, and mechanisms of the Atlantic meridional overturning circulation: A review. *Reviews of Geophysics*, 54(1), 5–63. <https://doi.org/10.1002/2015RG000493>
- Daniault, N., Mercier, H., Lherminier, P., Sarafanov, A., Falina, A., Zunino, P., et al. (2016). The northern North Atlantic Ocean mean circulation in the early 21st century. *Progress in Oceanography*, 146, 142–158. <https://doi.org/10.1016/j.pocean.2016.06.007>
- de Jong, M. F., de Steur, L., Fried, N., Bol, R., & Kritsotakis, S. (2020). Year-round measurements of the Irminger current: Variability of a two-core current system observed in 2014–2016. *Journal of Geophysical Research: Oceans*, 125(10), e2020JC016193. <https://doi.org/10.1029/2020JC016193>
- Desbruyères, D. G., Chafik, L., & Maze, G. (2021). A shift in the ocean circulation has warmed the subpolar North Atlantic Ocean since 2016. *Communications Earth & Environment*, 2(1), 48. <https://doi.org/10.1038/s43247-021-00120-y>
- Desbruyères, D. G., McDonagh, E. L., King, B. A., Garry, F. K., Blaker, A. T., Moat, B. L., & Mercier, H. (2014). Full depth temperature trends in the northeastern Atlantic through the early 21st century. *Geophysical Research Letters*, 41, 7971–7979. <https://doi.org/10.1002/2014GL061844>
- Desbruyères, D. G., McDonagh, E. L., King, B. A., & Thierry, V. (2017). *Global and full-depth ocean temperature trends during the early twenty-first century from Argo and repeat hydrography* (pp. 1985–1998). <https://doi.org/10.1175/JCLI-D-16-0396.1>
- Desbruyères, D. G., Purkey, S. G., McDonagh, E. L., Johnson, G. C., & King, B. A. (2016). Deep and abyssal ocean warming from 35 yr of repeat hydrography. *Geophysical Research Letters*, 43(19), 10356–10365. <https://doi.org/10.1002/2016GL070413>
- Devana, M. S., Johns, W. E., Houk, A., & Zou, S. (2021). Rapid freshening of Iceland Scotland overflow water driven by entrainment of a major upper ocean salinity anomaly. *Geophysical Research Letters*, 48(22), e2021GL094396. <https://doi.org/10.1029/2021GL094396>
- Dickson, B., Yashayaev, I., Meincke, J., Turrell, B., Dye, S., & Hølfort, J. (2002). Rapid freshening of the deep North Atlantic Ocean over the past four decades. *Nature*, 416(6883), 832–837. <https://doi.org/10.1038/416832a>
- Foppert, A., Rintoul, S. R., Purkey, S. G., Zilberman, N., Kobayashi, T., Sallée, J., et al. (2021). Deep Argo reveals bottom water properties and pathways in the Australian-Antarctic Basin. *Journal of Geophysical Research: Oceans*, 126(12), e2021JC017935. <https://doi.org/10.1029/2021jc017935>
- Fried, N., & de Jong, M. F. (2022). The role of the Irminger current in the Irminger Sea northward transport variability. *Journal of Geophysical Research: Oceans*, 127(3), e2021JC018188. <https://doi.org/10.1029/2021JC018188>
- Garry, F. K., McDonagh, E. L., Blaker, A. T., Roberts, C. D., Desbruyères, D. G., Frajka-Williams, E., & King, B. A. (2019). Model derived uncertainties in deep ocean temperature trends between 1990–2010. *Journal of Geophysical Research: Oceans*, 124(2), 1155–1169. <https://doi.org/10.1029/2018JC014225>
- Häkkinen, S., Rhines, P. B., & Worthen, D. L. (2015). Heat content variability in the North Atlantic Ocean in ocean reanalyses. *Geophysical Research Letters*, 42(8), 2901–2909. <https://doi.org/10.1002/2015GL063299>
- Hansen, B., & Østerhus, S. (2000). North Atlantic-Nordic Seas exchanges. *Progress in Oceanography*, 45(2), 109–208. [https://doi.org/10.1016/S0079-6611\(99\)00052-X](https://doi.org/10.1016/S0079-6611(99)00052-X)
- Holliday, N. P., Hughes, S. L., Bacon, S., Beszczynska-Möller, A., Hansen, B., Lavin, A., et al. (2008). Reversal of the 1960s–1990s freshening trend in the northeast North Atlantic and Nordic Seas. *Geophysical Research Letters*, 35(3), 1–5. <https://doi.org/10.1029/2007GL032675>
- IPCC, In Masson-Delmotte, V., Zhai, P., Pirani, A., Connors, S. L., Péan, C. (Eds.), et al. (2021). *Climate change 2021: The physical science basis. Contribution of Working Group I to the Sixth Assessment Report of the Intergovernmental Panel on Climate Change*. Cambridge University Press. Retrieved from <https://www.ipcc.ch/report/ar6/wg1/>
- Johns, W. E., Devana, M., Houk, A., & Zou, S. (2021). Moored observations of the Iceland-Scotland overflow plume along the eastern flank of the Reykjanes Ridge. *Journal of Geophysical Research: Oceans*, 126(8), e2021JC017524. <https://doi.org/10.1029/2021JC017524>
- Johnson, G. C. (2019). Deep Argo quantifies bottom water warming rates in the southwest Pacific basin. *Geophysical Research Letters*. <https://doi.org/10.1029/2018GL081685>
- Johnson, G. C., Cadot, C., Lyman, J. M., & McTaggart, K. E. (2020). Antarctic bottom water warming in the Brazil basin: 1990s through 2020, from WOCE to Deep Argo. *Geophysical Research Letters*, 47(18), e2020GL089191. <https://doi.org/10.1029/2020GL089191>

- Johnson, G. C., Lyman, J. M., & Loeb, N. G. (2016). Improving estimates of Earth's energy imbalance. *Nature Climate Change*, 6(7), 639–640. <https://doi.org/10.1038/nclimate3043>
- Johnson, G. C., Lyman, J. M., & Purkey, S. G. (2015). Informing Deep Argo array design using Argo and full-depth hydrographic section data. *Journal of Atmospheric and Oceanic Technology*, 32(11), 2187–2198. <https://doi.org/10.1175/JTECH-D-15-0139.1>
- Johnson, G. C., Purkey, S. G., Zilberman, N. V., & Roemmich, D. (2019). Deep Argo quantifies bottom water warming rates in the southwest Pacific basin. *Geophysical Research Letters*, 46(5), 2662–2669. <https://doi.org/10.1029/2018GL081685>
- Keeling, R. F., Körtzinger, A., & Gruber, N. (2009). Ocean deoxygenation in a warming world. *Annual Review of Marine Science*, 2(1), 199–229. <https://doi.org/10.1146/annurev.marine.010908.163855>
- Kobayashi, T. (2018). Rapid volume reduction in Antarctic Bottom Water off the Adélie/George V Land coast observed by deep floats. *Deep-Sea Research Part I: Oceanographic Research Papers*, 140, 95–117. <https://doi.org/10.1016/j.dsr.2018.07.014>
- Le Bras, I. A.-A., Straneo, F., Holte, J., & Holliday, N. P. (2018). Seasonality of freshwater in the east Greenland current system from 2014 to 2016. *Journal of Geophysical Research: Oceans*, 123(12), 8828–8848. <https://doi.org/10.1029/2018JC014511>
- Lozier, M. S., Li, F., Bacon, S., Bahr, F., Bower, A. S., Cunningham, S. A., et al. (2019). A sea change in our view of overturning in the subpolar North Atlantic. *Science*, 363(6426), 516–521. <https://doi.org/10.1126/science.aau6592>
- Mercier, H., Lherminier, P., Sarafanov, A., Gaillard, F., Daniault, N., Desbruyères, D., et al. (2015). Variability of the meridional overturning circulation at the Greenland-Portugal OVIDE section from 1993 to 2010. *Progress in Oceanography*, 132, 250–261. <https://doi.org/10.1016/j.pcean.2013.11.001>
- Petit, T., Mercier, H., & Thierry, V. (2018). First direct estimates of volume and water mass transports across the Reykjanes Ridge. *Journal of Geophysical Research: Oceans*, 6703–6719. <https://doi.org/10.1029/2018JC013999>
- Piron, A., Thierry, V., Mercier, H., & Caniaux, G. (2017). Gyre-scale deep convection in the subpolar North Atlantic Ocean during winter 2014–2015. *Geophysical Research Letters*, 44(3), 1439–1447. <https://doi.org/10.1002/2016GL071895>
- Purkey, S. G., & Johnson, G. C. (2010). Warming of global abyssal and deep Southern Ocean waters between the 1990s and 2000s: Contributions to global heat and sea level rise budgets. *Journal of Climate*, 23(23), 6336–6351. <https://doi.org/10.1175/2010JCLI3682.1>
- Racapé, V., Thierry, V., Mercier, H., & Cabanes, C. (2019). ISOW spreading and mixing as revealed by Deep-Argo floats launched in the Charlie Gibbs Fracture Zone. *Journal of Geophysical Research: Oceans*, 124(10), 6787–6808. <https://doi.org/10.1029/2019JC015040>
- Riser, S. C., Freeland, H. J., Roemmich, D., Wijffels, S., Troisi, A., Belbéoch, M., et al. (2016). Fifteen years of ocean observations with the global Argo array. *Nature Climate Change*, 6(2), 145–153. <https://doi.org/10.1038/nclimate2872>
- Robson, J., Ortega, P., & Sutton, R. (2016). A reversal of climatic trends in the North Atlantic since 2005. *Nature Geoscience*, 9(7), 513–517. <https://doi.org/10.1038/ngeo2727>
- Roemmich, D., Alford, M. H., Claustre, H., Johnson, K. S., King, B., Moun, J., et al. (2019). On the future of Argo: A global, full-depth, multi-disciplinary array. *Frontiers in Marine Science*. <https://doi.org/10.3389/fmars.2019.00439>
- Rühs, S., Oliver, E. C. J., Biastoch, A., Böning, C. W., Dowd, M., Getzlaff, K., et al. (2021). Changing spatial patterns of deep convection in the subpolar North Atlantic. *Journal of Geophysical Research: Oceans*, 126(7), e2021JC017245. <https://doi.org/10.1029/2021JC017245>
- Sallée, J.-B., Pellichero, V., Akhondas, C., Pauthenet, E., Vignes, L., Schmidtke, S., et al. (2021). Summertime increases in upper-ocean stratification and mixed-layer depth. *Nature*, 591(7851), 592–598. <https://doi.org/10.1038/s41586-021-03303-x>
- Sarafanov, A., Mercier, H., Falina, A., Sokov, E., & Lherminier, P. (2010). Cessation and partial reversal of deep water freshening in the northern North Atlantic: Observation-based estimates and attribution. *Tellus A: Dynamic Meteorology and Oceanography*, 62(1), 80–90. <https://doi.org/10.1111/j.1600-0870.2009.00418.x>
- Sarafanov, A., Sokov, A., Demidov, A., & Falina, A. (2007). Warming and salinification of intermediate and deep waters in the Irminger Sea and Iceland Basin in 1997–2006. *Geophysical Research Letters*, 34(23). <https://doi.org/10.1029/2007GL031074>
- Talley, L. D., Pickard, G. L., Emery, W. J., & Swift, J. H. (2011). Chapter 9—Atlantic Ocean. In L. D. Talley, G. L. Pickard, W. J. Emery, & J. H. Swift (Eds.), *Descriptive physical oceanography (sixth edition). An introduction* (pp. 245–301). Boston: Academic Press. <https://doi.org/10.1016/B978-0-7506-4552-2.10009-5>
- Tebaldi, C., Ranasinghe, R., Vourdoukas, M., Rasmussen, D. J., Vega-Westhoff, B., Kirezci, E., et al. (2021). Extreme sea levels at different global warming levels. *Nature Climate Change*, 11(9), 746–751. <https://doi.org/10.1038/s41558-021-01127-1>
- van Aken, H. M., & de Jong, M. F. (2012). Hydrographic variability of Denmark Strait overflow water near Cape Farewell with multi-decadal to weekly time scales. *Deep-Sea Research Part I: Oceanographic Research Papers*, 66, 41–50. <https://doi.org/10.1016/j.dsr.2012.04.004>
- Von Schuckmann, K., Cheng, L., Palmer, M. D., Hansen, J., Tassone, C., Aich, V., et al. (2020). Heat stored in the Earth system: Where does the energy go? *Earth System Science Data*, 12(3), 2013–2041. <https://doi.org/10.5194/essd-12-2013-2020>
- Waldman, R., Hirschi, J., Voltaire, A., Cassou, C., & Msadek, R. (2020). Clarifying the relation between AMOC and thermal wind: Application to the centennial variability in a coupled climate model. *Journal of Physical Oceanography*, 51(2), 343–364. <https://doi.org/10.1175/jpo-d-19-0284.1>
- Wong, A., Keeley, R., Carval, T., & the Argo Data Management Team. (2021). *Argo Quality Control Manual for CTD and Trajectory Data*.
- Yashayaev, I., & Loder, J. W. (2016). Recurrent replenishment of Labrador Sea water and associated decadal-scale variability. *Journal of Geophysical Research: Oceans*, 121(11), 8095–8114. <https://doi.org/10.1002/2016JC012046>
- Yashayaev, I., & Loder, J. W. (2017). Further intensification of deep convection in the Labrador Sea in 2016. *Geophysical Research Letters*, 44(3), 1429–1438. <https://doi.org/10.1002/2016GL071668>
- Zilberman, N. V., Roemmich, D. H., & Gilson, J. (2020). Deep-ocean circulation in the southwest Pacific Ocean interior: Estimates of the mean flow and variability using Deep Argo data. *Geophysical Research Letters*, 47(13), e2020GL088342. <https://doi.org/10.1029/2020GL088342>

**Warming-to-cooling reversal of overflow-derived water masses in the Irminger Sea during 2002-2021.**

Damien G. Desbruyères<sup>1</sup>, Eva Prieto Bravo<sup>1</sup>, Virginie Thierry<sup>1</sup>, Herlé Mercier<sup>1</sup>, Pascale Lherminier<sup>1</sup>, Cécile Cabanes<sup>1</sup>, Tiago C. Biló<sup>2</sup>, Nora Fried<sup>3</sup>, M. Femke De Jong<sup>3</sup>.

<sup>1</sup>University of Brest, CNRS, Ifremer, IRD, Laboratoire d'Océanographie Physique et Spatiale (UMR 6523 LOPS), Plouzané, France

<sup>2</sup>Scripps Institution of Oceanography, University of California San Diego.

<sup>3</sup>Department of Ocean Systems, NIOZ, Royal Netherlands Institute for Sea Research, Texel, The Netherlands

Corresponding author: Damien Desbruyères ([damien.desbruyeres@ifremer.fr](mailto:damien.desbruyeres@ifremer.fr))

**Contents of this file**

Figures S1

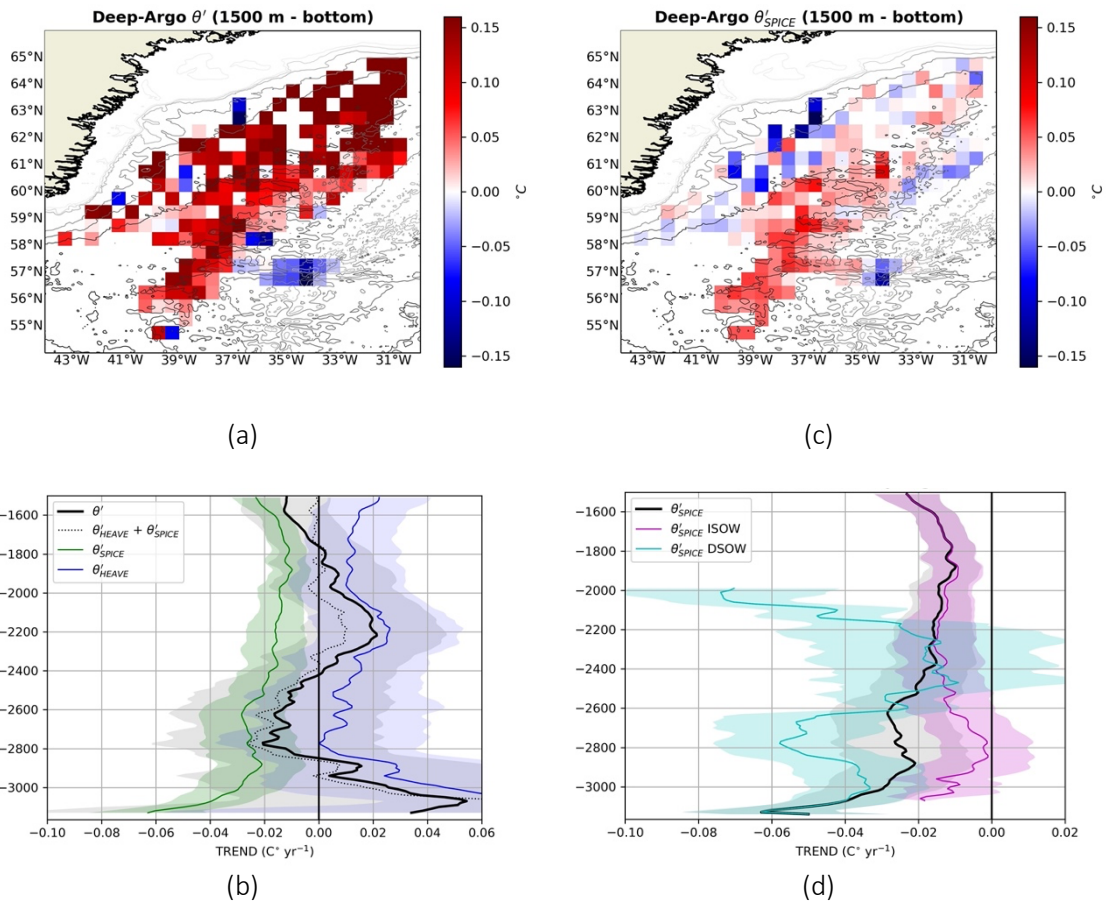


**Figure S1.** Same as Figure 4 (a, b, c, d) in the main manuscript but using the OV18 climatological product to obtain Deep-Argo-based temperature anomalies.